Lagrangian and Eulerian accelerations in turbulent stratified shear flows

Frank G. Jacobitz [1,*] and Kai Schneider [2,†]

[1]*Mechanical Engineering Department, Shiley-Marcos School of Engineering, University of San Diego,
5998 Alcalá Park, San Diego, California 92110, USA*

[2]*Aix-Marseille Université, CNRS, Centrale Marseille, Institut de Mathématiques de Marseille (I2M),
39 rue Joliot-Curie, 13453 Marseille Cedex 13, France*

The Lagrangian and Eulerian acceleration properties of fluid particles in homogeneous turbulence with uniform shear and uniform stable stratification are studied using direct numerical simulations. The Richardson number is varied from $Ri = 0$, corresponding to unstratified shear flow, to $Ri = 1$, corresponding to strongly stratified shear flow. The probability density functions (pdfs) of both Lagrangian and Eulerian accelerations have a stretched-exponential shape and they show a strong and similar influence on the Richardson number. The extreme values of the Eulerian acceleration are stronger than those observed for the Lagrangian acceleration. Geometrical statistics explain that the magnitude of the Eulerian acceleration is larger than its Lagrangian counterpart due to the mutual cancellation of the Eulerian and convective acceleration, as both vectors statistically show an antiparallel preference. A wavelet-based scale-dependent decomposition of the Lagrangian and Eulerian accelerations is performed. The tails of the acceleration pdfs grow heavier for smaller scales of turbulent motion. Hence the flatness increases with decreasing scale, indicating stronger intermittency at smaller scales. The joint pdfs of the Lagrangian and Eulerian accelerations indicate a trend to stronger correlations with increasing Richardson number and at larger scales of the turbulent motion. A consideration of the terms in the Navier-Stokes equation shows that the Lagrangian acceleration is mainly determined by the pressure-gradient term, while the Eulerian acceleration is dominated by the nonlinear convection term. A similar analysis is performed for the Lagrangian and Eulerian time rates of change of both fluctuating density and vorticity. The Eulerian time rates of change are observed to have extreme values substantially larger than those of their Lagrangian counterparts due to the advection terms in the advection-diffusion equation for fluctuating density and in the vorticity equation, respectively. The Lagrangian time rate of change of fluctuating vorticity is mainly determined by the vortex stretching and tilting term in the vorticity equation. Since the advection-diffusion equation for fluctuating density lacks a quadratic term, the Lagrangian time rate of change pdfs of fluctuating density show a more Gaussian shape, in particular, for large Richardson numbers. Hence, the Lagrangian acceleration and time rates of change of fluctuating density and vorticity reflect the dominant physics of the underlying governing equations, while the Eulerian acceleration and time rates of change are mainly determined by advection.

---

*jacobitz@sandiego.edu
†kai.schneider@univ-amu.fr

I. INTRODUCTION

An understanding of the Lagrangian acceleration properties of a fluid particle in turbulent motion is of fundamental importance and numerous applications exist in geophysical, environmental, and engineering flows. It aids in the study of transport and mixing, as well as in the characterization of geometric properties and intermittency at various scales of turbulent motion. As proposed by Tsinober *et al.* [1] and Tsinober [2], the Lagrangian description of turbulent flows may be a more natural approach to the study of turbulence, as it is more directly related to the dynamics of fluid particles, which are subjected to different forces, e.g., due to the fluctuating pressure gradient, buoyancy, viscous stresses, or other forcing terms.

Studying Lagrangian acceleration has some history. After early work by Heisenberg [3] and Yaglom [4], more recent studies range from theoretical investigations (e.g., Tsinober *et al.* [1], Tsinober [2]) to applications such as the modeling of particle dispersion (e.g., Pope [5]) highly relevant to turbulent combustion. Such studies are carried out using both experimental (e.g., La Porta *et al.* [6]) and computational (e.g., Yeung and Pope [7], Yeung [8], or Toschi and Bodenschatz [9]) approaches.

The majority of previous investigations focused on Lagrangian properties of isotropic turbulence. The Lagrangian acceleration was found to be strongly intermittent and heavy tails were observed in its probability density functions (pdfs). For example, extreme values as high as 1500 times the acceleration of gravity were observed for the Lagrangian acceleration of fluid particles by La Porta *et al.* [6] and numerical simulations by Toschi and Bodenschatz [9] confirmed these results.

Acceleration fluctuations and the different contributions have been studied by Pinsky *et al.* [10] and Tsinober *et al.* [1] in isotropic turbulence. Their work is motivated by the random Taylor hypothesis or sweeping decorrelation hypothesis "of small eddies in turbulent flow being passively "swept" past a stationary Eulerian observer [1]. It is based on the prediction of Tennekes [11] that states that the Lagrangian acceleration must be small, justified by considering Eulerian and Lagrangian time scales. He predicted that the rms value of the Lagrangian acceleration is a factor $Re_\lambda^{-1/2}$ smaller than the Eulerian value. Lin [12] showed that there is no general justification to extend Taylor's hypothesis to turbulent shear flow. He gives some perspectives that this may still hold for large wave numbers (small scales), which will be the topic of future work.

Tsinober *et al.* [1] analyzed direct numerical simulation data of isotropic turbulence for different Reynolds numbers and the Lagrangian acceleration, called the total acceleration in Tsinober's work, was decomposed into the Eulerian acceleration (called the local acceleration in [1]) and the convective contribution. Possible cancellation properties between the Eulerian and the convective contributions may yield reduced values of the Lagrangian acceleration. The authors found that the variance of the Lagrangian acceleration is much smaller than that of the Eulerian (local) acceleration and the advection term due to their strong negative alignment (or correlation) for sufficiently high R_λ, here 140. They also observed that the Lagrangian acceleration is strongly correlated with the pressure gradient. Their results are thus in support of the random Taylor hypothesis.

Note that the convective contribution of the acceleration becomes large when the flow is nonuniform, i.e., if the velocity changes along a streamline. The convective acceleration term is nonlinear, which causes mathematical difficulties in flow analysis; also, even in steady flow (which is perfect for Taylor's hypothesis), the convective acceleration can be large if spatial gradients of velocity are large. If it is antialigned with the local acceleration, it can be balanced and the total acceleration can still be small. This implies that the rate of Eulerian decorrelation is higher than that of Lagrangian decorrelation, which is crucial for two-point closures, see also the review on space-time correlations in turbulence by He *et al.* [13].

Many applications of Lagrangian dynamics target the transport and mixing of natural and anthropogenic substances in the geophysical environment. Such flows are often characterized by the presence of shear and stratification. A homogeneous turbulent stratified shear flow with a constant vertical stratification rate $S_\rho = \partial\varrho/\partial y$ and a constant vertical shear rate $S = \partial U/\partial y$ represents the simplest flow configuration in order to study the competing effects of shear and stratification.

This flow has been investigated extensively in the past. Experimental studies include work by Komori *et al.* [14], Rohr *et al.* [15], Piccirillo and Van Atta [16], and Keller and Van Atta [17]. Numerical simulations have been performed by Gerz *et al.* [18], Holt *et al.* [19], Jacobitz *et al.* [20], Jacobitz [21], and Portwood [22]. Hanazaki and Hunt [23] analyzed this flow using linear theory. More recently, the mixing properties of turbulent stratified shear flow have been considered by, for example, Salehipour *et al.* [24] and Venayagamoorthy and Koseff [25]. For a review, we refer to Gregg *et al.* [26].

More recently, Jacobitz *et al.* [27] considered Lagrangian and Eulerian accelerations in rotating and sheared homogeneous turbulence. It was found that the Lagrangian acceleration was mainly determined by the pressure-gradient term in the Navier-Stokes equation, while the Eulerian acceleration shows stronger tails due to the advection term. In the case of strong rotation, linear effects are dominant and the Lagrangian acceleration pdf takes an approximately Gaussian shape. A comparison of linear theory with direct numerical simulation of rotating and sheared homogeneous turbulence was performed by Salhi *et al.* [28].

The goal of this work is to investigate the acceleration statistics and to analyze the different contributions to the acceleration in turbulent stratified shear flows using direct numerical simulations. A key question is the understanding of the properties of Lagrangian acceleration fluctuations and their Eulerian counterpart and the influence of the Richardson number.

In the following, the numerical approach taken in this study is introduced first. Then the Richardson number dependence of the Lagrangian and Eulerian acceleration pdfs is presented along with geometrical statistics of the alignment angles of the different contributions. Using a wavelet-based scale-dependent decomposition, the Lagrangian and Eulerian accelerations are studied at various scales of the turbulent motion and their spatial fluctuations are analyzed. The corresponding Lagrangian and Eulerian time rates of change pdfs for the fluctuating density are discussed. Finally, a summary and conclusion of the present work is provided. Results for the Lagrangian and Eulerian time rates of change for the fluctuating vorticity as well as the Lagrangian and Eulerian acceleration component are discussed in the Appendixes.

II. APPROACH

In this section, the equations of motion and their direct numerical solution are described, variance estimates for the Lagrangian and Eulerian accelerations are given, the wavelet-based scale-dependent decomposition of the accelerations is introduced, and geometrical statistics to study the alignment of the different acceleration contributions are motivated.

A. Equations of motion

The mean flow with velocity (U, V, W) and density ϱ considered in this study has a constant vertical shear rate $S = \partial U / \partial y$ and a constant vertical stratification rate $S_\rho = \partial \varrho / \partial y$, respectively,

$$U = Sy, \quad V = W = 0, \quad \varrho = \rho_0 + S_\rho y, \tag{1}$$

where ρ_0 is the ambient density.

This study is based on the incompressible Navier-Stokes equations for the fluctuating velocity and an advection-diffusion equation for the fluctuating density:

$$\nabla \cdot \boldsymbol{u} = 0, \tag{2}$$

$$\frac{\partial \boldsymbol{u}}{\partial t} + \boldsymbol{u} \cdot \nabla \boldsymbol{u} + Sy \frac{\partial \boldsymbol{u}}{\partial x} + Sv\boldsymbol{e}_x, = -\frac{1}{\rho_0} \nabla p - \frac{g}{\rho_0} \rho \boldsymbol{e}_y + \nu \nabla^2 \boldsymbol{u}, \tag{3}$$

$$\frac{\partial \rho}{\partial t} + \boldsymbol{u} \cdot \nabla \rho + S_\rho v = \alpha \nabla^2 \rho. \tag{4}$$

TABLE I. Overview of the simulation cases, including the Richardson number Ri, the shear rate S, the Brunt–Väisälä frequency N, the Taylor-microscale Reynolds number Re_λ, The viscosity ν, the turbulent velocity fluctuation q, the dissipation rate of kinetic energy ϵ, the cutoff wave number $k_{max}\eta$, the overturning scale $L_{overturn}$, the Ellison scale $L_{Ellison}$, the Ozmidov scale $L_{Ozmidov}$, the Taylor microscale λ, and the Kolmogorov scale η. All values are given at nondimensional time $St = 10$. All symbols are defined in the text.

	Ri				
	0	0.1	0.2	0.5	1
S	5.3345	5.3345	5.3345	5.3345	5.3345
N	0.0000	1.6869	2.3856	3.7720	5.3345
Re_λ	156.90	104.08	76.60	42.84	32.83
ν	0.0010	0.0010	0.0010	0.0010	0.0010
q	1.5856	1.0779	0.7969	0.4428	0.3028
ϵ	1.2838	0.6230	0.3436	0.1048	0.0390
$k_{max}\eta$	1.1992	1.4368	1.6673	2.2437	2.8723
$L_{overturn}$	3.1052	2.0101	1.4728	0.8288	0.7119
$L_{Ellison}$	0.2619	0.1835	0.1324	0.0619	0.0312
$L_{Ozmidov}$	N/A	0.3603	0.1591	0.0442	0.0160
λ	0.09895	0.09656	0.09613	0.09675	0.10841
η	0.00528	0.00633	0.00735	0.00988	0.01265

Here, $\boldsymbol{u} = (u, v, w)$ is the fluctuating velocity, p the fluctuating pressure, ρ the fluctuating density, ν the kinematic viscosity, and α the scalar diffusivity. Taking the curl of the momentum equation, (3), leads to the vorticity equation:

$$\frac{\partial \boldsymbol{\omega}}{\partial t} + \boldsymbol{u} \cdot \nabla \boldsymbol{\omega} + \nabla \times \left(Sy \frac{\partial \boldsymbol{u}}{\partial x} + Sv\boldsymbol{e}_x \right) = \boldsymbol{\omega} \cdot \nabla \boldsymbol{u} - \nabla \times \left(\frac{g}{\rho_0} \rho \boldsymbol{e}_y \right) + \nu \nabla^2 \boldsymbol{\omega}. \tag{5}$$

B. Numerical approach

For their numerical solution, the equations of motion, (2)–(4), are transformed into a frame of reference moving at the mean velocity (see Rogallo [29]). This transformation enables the application of periodic boundary conditions for the fluctuating components of velocity and density. A spectral collocation method is used for the spatial discretization and the solution is advanced in time with a fourth-order Runge-Kutta scheme.

Table I provides an overview of the simulations performed for this study. The Richardson number $Ri = N^2/S^2$ is varied from $Ri = 0$, corresponding to unstratified shear flow, to $Ri = 1$, corresponding to strongly stratified shear flow. While both the mean shear rate $S = \partial U/\partial y$ and the mean stratification rate $S_\rho = \partial \varrho/\partial y$ are constant for a given simulation, the Richardson number variation is obtained by a change of the Brunt-Väisälä frequency N with $N^2 = -g/\rho_0 S_\rho$, while keeping the mean shear rate S constant.

The initial conditions are taken from a separate simulation of isotropic turbulence without density fluctuations, which was allowed to develop for approximately one eddy turnover time. The initial values of the Taylor-microscale Reynolds number $Re_\lambda q\lambda/\nu = 89$ and the shear number $SK/\epsilon = 2$ are fixed. Here q is the rms of the fluctuating velocity with $q^2 = \overline{u_i u_i}$, λ the Taylor microscale with $\lambda^2 = 5q^2\nu/\epsilon$, $K = q^2/2$ the kinetic energy, and $\epsilon = \nu \overline{\partial u_j/\partial x_k \partial u_j/\partial x_k}$ the dissipation rate.

Table I provides an overview of the eventual values of Re_λ, q, and ϵ at time $St = 10$. The table also lists the values of a variety of length scales, including the overturning scale $L_{overturn} = q^3/\epsilon$, the Ellison scale $L_{Ellison} = \rho/S_\rho$, the Ozmidov scale $L_{Ozmidov}$ with $L_{Ozmidov}^2 = \epsilon/N^3$, the Taylor microscale λ, and the Kolmogorov scale η with $\eta^4 = \nu^3/\epsilon$, indicating an appropriate resolution of the simulations at $St = 10$ at both the large and the small scales of the turbulent motion.

The simulations are performed on a parallel computer using $512 \times 512 \times 512$ grid points. To increase the resolution, instead of the classical dealiasing with a cutoff at 2/3 of the maximum wave number, a cosine-filter dealiasing is applied. The cosine filter is only applied to wave numbers larger than 2/3 of the maximum wave number. Its transfer function starts with 1 at 2/3 of the maximum wave number, goes to 0 at the maximum wave number, and follows the shape of the first quarter of the cosine function period. The maximum wave number k_{max} can be defined when the cosine is equal to the value 1/2. For the current resolution with $N = 512$ we thus have $k_{max} = 227$ (instead of the value 170 obtained for classical dealiasing). All simulations are well resolved and we have $k_{max}\eta > 1.2$ in the eventual evolution for the unstratified case. A discussion of the influence of dealiasing in pseudospectral codes is given by Hou and Li [30]. The authors show that the classical 2/3 rule does not necessarily yield the best results and other filtering techniques, different from the cosine-dealiasing used here, are more efficient, supporting our choice.

C. Variance estimates for the Lagrangian and Eulerian accelerations in stratified shear flow

The Lagrangian and Eulerian accelerations are defined as

$$a_L = \frac{\partial \boldsymbol{u}}{\partial t} + \boldsymbol{u} \cdot \nabla \boldsymbol{u} \quad \text{and} \quad a_E = \frac{\partial \boldsymbol{u}}{\partial t}, \tag{6}$$

respectively. Both accelerations are computed as a volume average at a fixed time, which is an appropriate choice for homogeneous flows. The effects of shear and buoyancy are considered as external forces.

In [27] we provided estimates of the variances of the Lagrangian and Eulerian accelerations, writing the Navier-Stokes equations in the form

$$\frac{\partial \boldsymbol{u}}{\partial t} = -\boldsymbol{N} - \boldsymbol{\Pi} - \boldsymbol{\Lambda}, \tag{7}$$

where the terms on the right-hand side are given by

$$
\begin{aligned}
\boldsymbol{N} &= \boldsymbol{a}_C = \boldsymbol{u} \cdot \nabla \boldsymbol{u}, \\
\boldsymbol{\Pi} &= \boldsymbol{a}_P = \nabla(p/\rho_0), \\
\boldsymbol{\Lambda} &= \boldsymbol{\Lambda}_S + \boldsymbol{\Lambda}_B + \boldsymbol{\Lambda}_V = Sv\boldsymbol{e}_x + \frac{g}{\rho_0}\rho\boldsymbol{e}_y - \nu\nabla^2\boldsymbol{u}.
\end{aligned} \tag{8}
$$

Here, $\boldsymbol{N}$ is the nonlinear or advection term, $\boldsymbol{\Pi}$ the pressure-gradient term, and $\boldsymbol{\Lambda}$ the linear term with contributions from shear, buoyancy, and viscous effects. The notation $\boldsymbol{a}_C$ for the nonlinear term and $\boldsymbol{a}_P$ for the pressure gradient match the notation of Tsinober *et al.* [1] to denote the convective and pressure contributions, respectively, to the accelerations.

According to [27] we have also, in the case of stratified shear flow, the identity

$$\langle\|\boldsymbol{N} + \boldsymbol{\Pi} + \boldsymbol{\Lambda}\|^2\rangle = \langle\|\boldsymbol{N} + \boldsymbol{\Lambda}\|^2\rangle - \langle\|\boldsymbol{\Pi}\|^2\rangle. \tag{9}$$

Here, $\|\cdot\|$ denotes the magnitude of a vector and $\langle\cdot\rangle$ the volume average for a homogeneous field.

This directly implies the exact identities for the variances of the Eulerian acceleration $\boldsymbol{a}_E$ (called the local acceleration by Tsinober *et al.* [1]),

$$a_E^2 \equiv \left\langle\|\frac{\partial \boldsymbol{u}}{\partial t}\|^2\right\rangle = \langle\|\boldsymbol{N} + \boldsymbol{\Pi} + \boldsymbol{\Lambda}\|^2\rangle = \langle\|\boldsymbol{N} + \boldsymbol{\Lambda}\|^2\rangle - \langle\|\boldsymbol{\Pi}\|^2\rangle, \tag{10}$$

and of the Lagrangian acceleration $\boldsymbol{a}_L$ (called the total acceleration by Tsinober *et al.* [1]),

$$a_L^2 \equiv \left\langle\|\frac{\partial \boldsymbol{u}}{\partial t} + \boldsymbol{u} \cdot \nabla \boldsymbol{u}\|^2\right\rangle = \langle\|\boldsymbol{\Pi} + \boldsymbol{\Lambda}\|^2\rangle. \tag{11}$$

The variance estimates provided in [27] for rotating shear flows are now extended to stratified shear flows, again with the underlying assumption and crucial simplification of isotropy of the flow.

The main difference arises in the linear term $\mathbf{\Lambda}$, which now includes a buoyancy force, instead of a Coriolis force. Neglecting the friction force, the variance of the linear term can be written as

$$\Lambda^2 = \frac{1}{3}S^2\left[1 + 3\left(\frac{g}{\rho_0}\right)^2\frac{1}{S^2}\frac{\rho^2}{u^2}\right]u^2. \tag{12}$$

Using the ratio of potential to kinetic energy

$$\frac{K_\rho}{K} = \frac{-\frac{1}{2}\frac{g}{\rho_0}\frac{\rho^2}{S_\rho}}{\frac{1}{2}u^2} = -\frac{g}{\rho_0}\frac{1}{S_\rho}\frac{\rho^2}{u^2}, \tag{13}$$

the variance for the linear term can be written as

$$\Lambda^2 = \frac{1}{3}S^2\left[1 + 3Ri\frac{K_\rho}{K}\right]u^2. \tag{14}$$

Hence, the variance estimate of the linear term retains the ratio of potential to kinetic energy.

D. Scale-dependent decomposition of Lagrangian and Eulerian accelerations

To gain insight into the scale dependence of the Lagrangian and Eulerian accelerations, we decompose both accelerations into an orthogonal wavelet series. Wavelets are well-localized functions in space and in scale (or wave number) (see, e.g., [31]), and different wavelet-based diagnostics, including the scale-dependent energy distribution and its spatial fluctuations, intermittency measures such as the scale-dependent flatness and anisotropy measures, have been proposed. For a review we refer the reader to [32].

We consider a generic vector field $\boldsymbol{a} = (a_1, a_2, a_3)$ at a fixed instant in time and decompose each component $a_\alpha(\boldsymbol{x})$ into an orthogonal wavelet series,

$$a_\alpha(\boldsymbol{x}) = \sum_\lambda \widetilde{a}_\lambda^\alpha \psi_\lambda(\boldsymbol{x}), \tag{15}$$

where the wavelet coefficients are given by the scalar product $\widetilde{a}^\alpha = \langle a_\alpha, \psi_\lambda \rangle$. The wavelets ψ_λ with the multi-index $\lambda = (j, \boldsymbol{i}, d)$ are well localized in scale $L_0 2^{-j}$ (where L_0 corresponds to the size of the computational domain), around position $L_0\boldsymbol{i}/2^j$, and oriented in one of the seven directions $d = 1, \dots, 7$, respectively. The scale is directly related to the wave number $k_j = k_0 2^j$, where k_0 is the centroid wave number of the chosen wavelet family. For Coiflet 12 wavelets used in the present work we have $k_0 = 0.77$. Large scales correspond to small values of the scale index j and to a well-localized wavelet in Fourier space around wave number k_j. In contrast, for small scales, which correspond to large values of j, the wavelet becomes less localized in Fourier space around the mean wave number k_j.

Reconstructing the three components a^α at scale 2^{-j} by summing only over the position $\boldsymbol{i}$ and direction d indices in Eq. (15) yields the acceleration $\boldsymbol{a}^j$ at scale index j. In terms of filtering the acceleration at a given scale corresponds to a bandpass-filtered field, with a bandpass filter having a constant relative bandwidth. This means that the filter width becomes larger at larger wave numbers, corresponding to decreasing scale. By construction we have $\boldsymbol{a} = \sum_j \boldsymbol{a}^j$, where the $\boldsymbol{a}^j$ are mutually orthogonal.

The scale-dependent moments, including the scale-dependent flatness and scale-dependent pdfs, can thus be computed from $\boldsymbol{a}^j$ using classical statistical estimators. For instance, the qth-order moment of $\boldsymbol{a}^j(\boldsymbol{x})$ can be defined by

$$M_q[\boldsymbol{a}^j] = \langle (\boldsymbol{a}^j)^q \rangle, \tag{16}$$

and by construction the mean value vanishes, $\langle \boldsymbol{a}^j \rangle = 0$. The moments are thus central moments. These scale-dependent moments are directly related to the qth-order structure functions [33] where the increment size is 2^{-j}.

The scale-dependent flatness, which measures the intermittency of $\boldsymbol{a}^j$ at scale 2^{-j}, is defined by

$$Fl[\boldsymbol{a}^j] = \frac{M_4[\boldsymbol{a}^j]}{(M_2[\boldsymbol{a}^j])^2}. \tag{17}$$

For a Gaussian distribution the flatness equals 3 at all scales.

E. Geometrical statistics

To understand the magnitude of Eulerian and Lagrangian accelerations, we statistically assess, following Tsinober et al. [1], the alignment properties of $\boldsymbol{a}_E$, $\boldsymbol{a}_C = \boldsymbol{N}$, and its sum corresponding to the Lagrangian acceleration $\boldsymbol{a}_L = \boldsymbol{a}_E + \boldsymbol{a}_C$. For convenience, we partly use the notation introduced in [1] in this section. When the vectors of the Eulerian acceleration $\boldsymbol{a}_E$ and the convective terms $\boldsymbol{a}_C$ are antiparallel, then the magnitude of the Lagrangian acceleration $\boldsymbol{a}_L$ is small compared to those of the Eulerian and convective contributions, since

$$\langle \boldsymbol{a}_L, \boldsymbol{a}_L \rangle = \langle \boldsymbol{a}_E + \boldsymbol{a}_C, \boldsymbol{a}_E + \boldsymbol{a}_C \rangle = \langle \boldsymbol{a}_E, \boldsymbol{a}_E \rangle + \langle \boldsymbol{a}_C, \boldsymbol{a}_C \rangle + 2\cos(\boldsymbol{a}_E, \boldsymbol{a}_C) \, ||\boldsymbol{a}_E|| \, ||\boldsymbol{a}_C||. \tag{18}$$

Here $\langle \cdot, \cdot \rangle$ denotes the scalar product.

If $\boldsymbol{a}_E$ and $\boldsymbol{a}_C$ are antialigned the cosine is negative and the norm of $\boldsymbol{a}_E + \boldsymbol{a}_C$ is minimal. To verify the random Taylor hypothesis Tsinober et al. [1] computed the cosine of the angle of the Eulerian acceleration and the convective term, motivated by the prediction of Tennekes [11] that the Lagrangian acceleration must be small for the hypothesis to hold. We expect this result to hold with modification due to shear and stratification.

For the pressure gradient term $\boldsymbol{a}_P = \boldsymbol{\Pi}$, the alignment with the Eulerian and Lagrangian acceleration can be likewise assessed. For sufficiently high Reynolds numbers we anticipate a strong antialignment of $\boldsymbol{a}_P$ with $\boldsymbol{a}_L$, showing that the flow is driven by the pressure gradients and that linear effects are negligible. However, buoyancy may change this result for strong stratification and its impact will be assessed using the simulation results.

For Gaussian divergence-free random fields Tsinober et al. [1] found similar alignment properties and they concluded that the cancellation of $\boldsymbol{a}_E$ and $\boldsymbol{a}_C$ is mostly a kinematic effect and not due to Navier-Stokes dynamics. A justification of these findings is given by Millionshchikow's zero–fourth cumulant hypothesis [34], which decomposes fourth-order moments into a series of second-order moments.

III. RESULTS

In this section, the flow evolution is briefly described first. Then results for the probability density functions of the Lagrangian and Eulerian accelerations are provided, related to the remaining terms in the Navier-Stokes equations, and their scale-dependent properties are presented. A similar analysis is performed for the Lagrangian and Eulerian time rates of change of fluctuating density and in Appendix A also for fluctuating vorticity. In the following, the accelerations and time rates of change are analyzed at the instant $St = 10$. Table I provides an overview of the series of five simulations performed.

A. Turbulence evolution

In order to provide a context for the present study, the energetics of the flow is briefly discussed. More details on turbulent stratified shear flows can be found in [20] and [21].

Figure 1 (left) shows the evolution of the turbulent kinetic energy normalized by its initial value K/K_0. All cases result in an initial decay phase due to the isotropic initial conditions. Then, as the Richardson number Ri is increased, the eventual evolution of the turbulent kinetic energy changes from growth to decay, with a critical value of $Ri_{cr} \approx 0.15$.
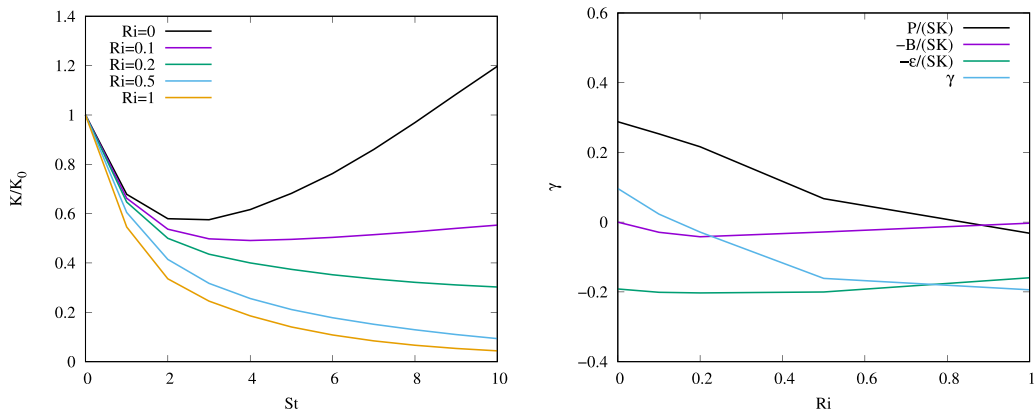
FIG. 1. Evolution of the turbulent kinetic energy K in nondimensional time St (left) and dependence of the normalized production rate $P/(SK)$, buoyancy flux $B/(SK)$, and dissipation rate $\epsilon/(SK)$ on the Richardson number at $St = 10$ (right).

The normalized transport equation for the turbulent kinetic energy evolution can be written as

$$\gamma = \frac{1}{SK}\frac{dK}{dt} = \frac{P}{SK} - \frac{B}{SK} - \frac{\epsilon}{SK}. \tag{19}$$

Here, γ is the growth rate of the turbulent kinetic energy, $P/(SK)$ is the normalized production term with $P = -S\overline{u_1 u_2}$, $B/(SK)$ is the normalized buoyancy flux with $B = g/\rho_0\overline{u_2\rho}$, and $\epsilon/(SK)$ is the normalized dissipation rate.

Figure 1 (right) shows the dependence of $P/(SK)$, $B/(SK)$, $\epsilon/(SK)$, and γ on the Richardson number Ri at nondimensional time $St = 10$. The normalized production rate $P/(SK)$ decreases with increasing Richardson number Ri and it assumes a slightly negative value for large-Ri cases, indicating a positive Reynolds shear stress (or counter-gradient flux). The normalized buoyancy flux $B/(SK)$ remains relatively small and it converts kinetic to potential energy for most of the Ri range. The normalized dissipation rate $\epsilon/(SK)$ remains relatively unaffected by the Ri variation. The growth rate γ follows the trend of the normalized production rate $P/(SK)$, offset by the contributions of $B/(SK)$ and $\epsilon/(SK)$. Note that positive values of γ correspond to an increase in K, while a negative value of γ indicates decay of the turbulent kinetic energy.

The evolution of the ratio of potential to kinetic energy is shown in Fig. 2 (left). The simulations are initialized without potential energy and a strong initial growth is observed. The ratio of potential to kinetic energy eventually reaches an approximately constant value, which still depends on the Richardson number Ri. This dependence of the ratio K_ρ/K on Ri at nondimensional time $St = 10$ is presented in Fig. 2 (right). The ratio K_ρ/K first increases strongly and then reaches a maximum of $K_\rho/K \approx 0.3$ for Ri = 1.

B. Lagrangian and Eulerian accelerations

Figure 3 (top) shows the probability distribution functions of the Lagrangian acceleration $\boldsymbol{a}_L$ (left) and of the Eulerian acceleration $\boldsymbol{a}_E$ (right). The pdfs of both accelerations have stretched-exponential shapes and they exhibit a strong and similar influence on the Richardson number Ri. For small Ri, the extreme values of the Eulerian acceleration are above those of the Lagrangian acceleration, which is consistent with previous observations for sheared and rotating turbulence [27] and likewise observed for isotropic turbulence by Tsinober *et al.* [1].

Figure 3 (bottom) shows the pdfs normalized with the corresponding standard deviations of the two accelerations. For a core region of about five standard deviations, both the Lagrangian and the Eulerian accelerations show approximately the same shape. The tails of the pdfs of both
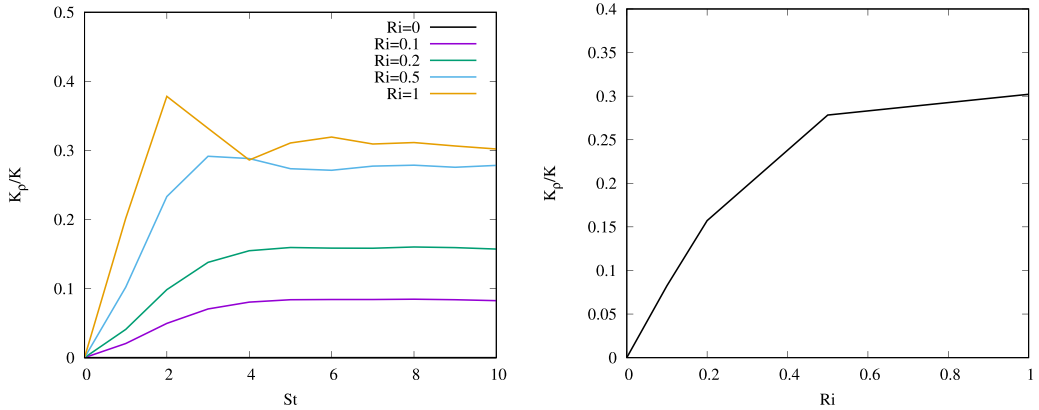
FIG. 2. Evolution of the ratio of turbulent potential to kinetic energy K_ρ/K in nondimensional time St (left) and dependence of this ratio on the Richardson number at $St = 10$ (right).
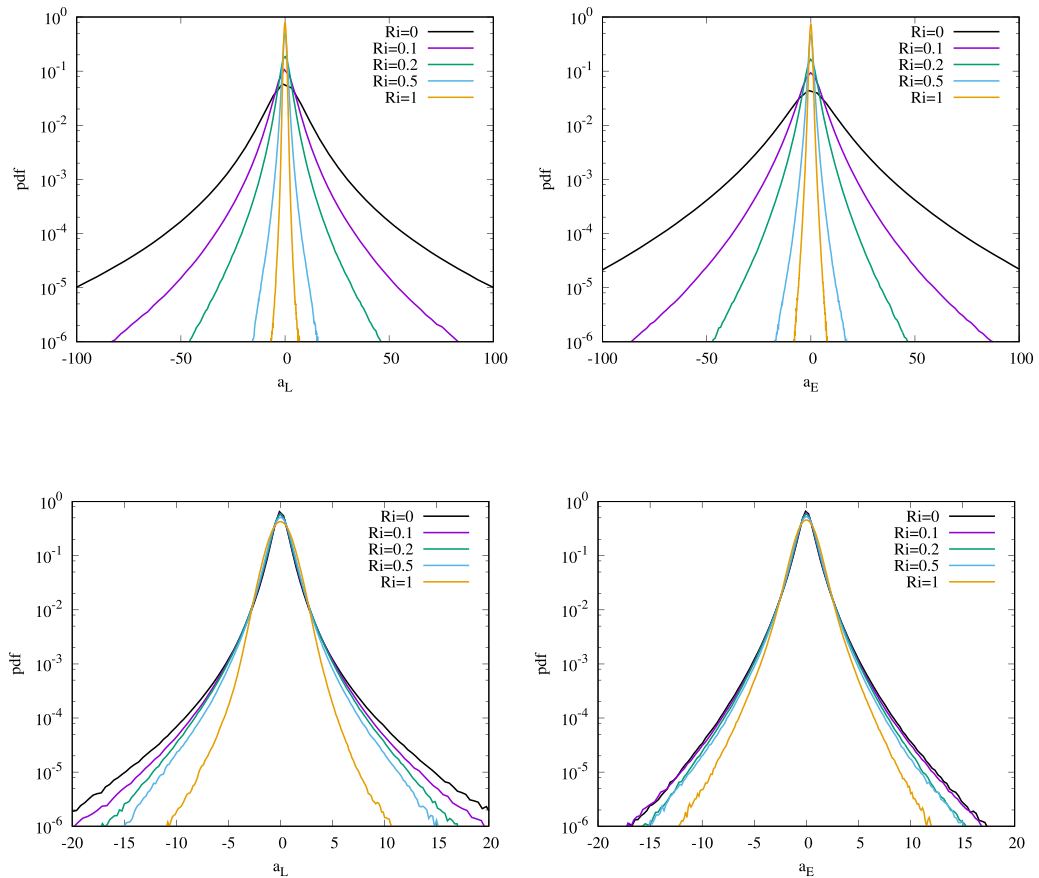

FIG. 3. Pdfs (top) and pdfs normalized with the corresponding standard deviations (bottom) of Lagrangian acceleration $\boldsymbol{a}_L$ (left) and Eulerian acceleration $\boldsymbol{a}_E$ (right) at nondimensional time $St = 10$. Note that all pdfs are estimated using histograms with 100 bins, and they are plotted in log-lin representation. Note that pdfs for the vector quantities are shown.

TABLE II. Lagrangian acceleration statistics at nondimensional time $St = 10$ showing the rms of the Lagrangian acceleration a_L, the flatness Fl_{a_L}, and the ratio of the componentwise variances and the total variance. The variance and flatness values of the time rates of change of fluctuating density s_L and Fl_{s_L} and fluctuating vorticity c_L and Fl_{c_L} are likewise listed.

			Ri		
	0	0.1	0.2	0.5	1
a_L	19.427	9.833	5.519	1.808	0.942
Fl_{a_L}	27.814	26.041	13.115	9.364	4.111
a_{Lx}^2/a_L^2	0.335	0.318	0.306	0.320	0.327
a_{Ly}^2/a_L^2	0.325	0.327	0.331	0.356	0.390
a_{Lz}^2/a_L^2	0.340	0.355	0.363	0.324	0.242
s_L	0.00117	0.00070	0.00091	0.00101	0.00119
Fl_{s_L}	7.220	6.148	5.152	3.989	3.249
c_L	490.484	232.508	128.472	44.395	19.725
Fl_{c_L}	65.574	53.766	21.168	14.123	9.177

accelerations weaken with increasing Ri. For small Ri, the tails of the Lagrangian acceleration are heavier than the tails of the Eulerian acceleration.

Tables II and III provide statistical information on the Lagrangian and Eulerian accelerations as a function of the Richardson number at nondimensional time $St = 10$. The magnitudes (rms values) of both accelerations decrease with increasing Ri and the magnitude of $\boldsymbol{a}_E$ always remains larger than the magnitude of $\boldsymbol{a}_L$, also observed for isotropic turbulence by Tsinober et al. [1]. At small Ri, the heavier tails observed for the normalized pdfs of $\boldsymbol{a}_L$ compared to $\boldsymbol{a}_E$ result in a larger flatness of the Lagrangian acceleration pdf compared to its Eulerian counterpart. The flatness values of both accelerations generally decrease with increasing Ri, indicating a decreased importance of nonlinear effects which is related to the decreasing Reynolds number. However, unlike in the presence of strong rotation considered in [27], the flatness values do not reach a value close to 3, characteristic for a Gaussian distribution, in the case of strong stratification. For Ri = 0 the flatness values of $\boldsymbol{a}_L$ and $\boldsymbol{a}_E$ are comparable with DNS data on isotropic turbulence [2] at $Re_\lambda = 140$, where the values of 24.4 and 12.8 were found, while we find, respectively, 27.81 and 14.41 in the case of pure shear. Note that for the variances Tsinober et al. [1] found the values (normalized with $\epsilon^{3/2}\nu^{-1/2} = 24.84$,

TABLE III. Eulerian acceleration statistics at nondimensional time $St = 10$ showing the rms of the Eulerian acceleration a_E, the flatness Fl_{a_E}, and the ratio of the componentwise variances and the total variance. The variance and flatness values of the time rates of change fluctuating density s_E and Fl_{s_E} and of fluctuating vorticity c_E and Fl_{c_E} are likewise listed.

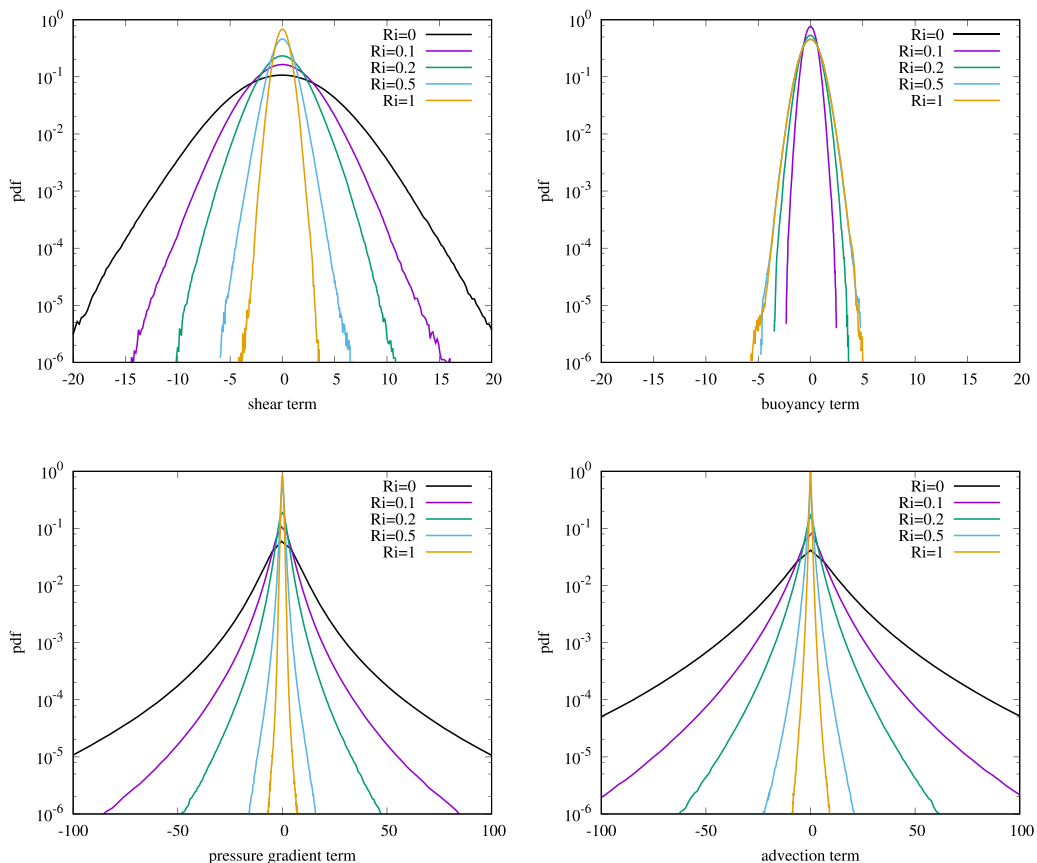|			Ri		
	0	0.1	0.2.	0.5.	1
a_E	26.100	11.689	6.258	1.975	1.075
Fl_{a_E}	14.414	13.413	11.028	9.510	5.691
a_{Ex}^2/a_E^2	0.302	0.320	0.339	0.408	0.434
a_{Ey}^2/a_E^2	0.329	0.312	0.292	0.261	0.273
a_{Ez}^2/a_E^2	0.369	0.368	0.369	0.331	0.293
s_E	0.00577	0.00239	0.00231	0.00138	0.00129
Fl_{s_E}	24.992	24.624	21.960	16.053	5.475
c_E	2,020.203	781.238	372.030	91.830	34.461
Fl_{c_E}	37.813	35.619	27.855	24.893	17.724

FIG. 4. Pdfs of the shear (top left), buoyancy (top right), pressure-gradient (bottom left), and advection (bottom right) terms in the Navier-Stokes equations at nondimensional time $St = 10$.

where $\epsilon = 1.20$ and $\nu = 0.0028$) of 2.75 for a_L and 8.19 for a_E (and 10.96 for a_C), while we find respectively the values 8.20 for a_L and 14.81 for a_E (and 22.39 for a_C) in the case of pure shear using the same normalization with $\epsilon^{3/2}\nu^{-1/2}$. This shows that the order is consistent and the values are comparable.

Figure 4 shows pdfs of the shear term (top left), the buoyancy term (top right), the pressure-gradient term (bottom left), and the advection term (bottom right) in the Navier-Stokes equation. The shear and buoyancy terms depend linearly on the fluctuating velocity components and density and their pdfs hence have a Gaussian shape. While the magnitude of the shear term pdf decreases with increasing Ri, the magnitude of the buoyancy term pdf increases. The pdfs of the pressure-gradient and advection terms show a stretched-exponential shape due to the quadratic nature of the terms. The magnitudes of both terms decrease with increasing Ri. For small Ri, the pressure-gradient and advection terms clearly dominate the shear and buoyancy terms, but this dominance somewhat diminishes with increasing Ri. Hence, the pressure-gradient term is the generally dominant contribution to the Lagrangian acceleration, while the advection term is important for the Eulerian acceleration.

Table IV lists the variances of the contributions to the linear term from the shear term Λ_S^2, the buoyancy term Λ_B^2, and the viscous term Λ_V^2. An estimate of the variance of the linear term Λ_{DNS}^2 is computed using the triangle inequality. The table also lists the variance of the velocity q^2, the ratio of potential to kinetic energies K_ρ/K, and a theoretical estimate of the linear term Λ^2 based on Eq. (14)

TABLE IV. Variance of the contributions to the linear term from the shear term Λ_S^2, buoyancy term Λ_B^2, and viscous term Λ_V^2, an estimate for the variance of the linear term using the triangle inequality Λ_{DNS}^2, the variance of the velocity q^2, the ratio of potential to kinetic energies K_ρ/K, and an estimate for the linear term Λ^2 given in Eq. (14) at nondimensional time $St = 10$.

	Ri				
	0	0.1	0.2	0.5	1
Λ_S^2	14.5746	6.3796	3.2517	0.8430	0.3596
Λ_B^2	0.0000	0.2728	0.5681	0.7767	0.7886
Λ_V^2	6.8850	2.5158	1.1384	0.2568	0.0723
Λ_{DNS}^2	21.4596	9.1682	4.9581	1.8764	1.2205
q^2	2.5142	1.1619	0.6350	0.1961	0.0917
K_ρ/K	0.0000	0.0825	0.1571	0.2783	0.3021
Λ^2	23.8427	11.2910	6.5897	2.6358	1.6579

at nondimensional time $St = 10$. The variances of the linear term computed from the simulation results Λ_{DNS}^2 and the theoretical estimate Λ^2 agree well, despite the assumption of isotropy used in the derivation of Eq. (14). The variance of the linear term decreases with increasing Richardson number Ri. The Taylor-microscale Reynolds number Re_λ listed in Table I yields a measure of the general importance of nonlinear effects in a turbulent flow. Re_λ decreases with increasing Ri. The results suggest that nonlinear effects contribute the least to the turbulence evolution for the case with a Richardson number Ri = 1.

The joint pdfs of the Lagrangian and Eulerian accelerations are shown in Fig. 5 for two cases with Richardson numbers Ri = 0.1 (left) and Ri = 1 (right) at nondimensional time $St = 10$. The correlation between Lagrangian and Eulerian accelerations is observed to increase with increasing Ri. The stronger correlation of the Eulerian and Lagrangian acceleration for Ri = 1 is due to the reduced nonlinearity.

In order to quantify this observation, the Pearson product-moment correlation coefficient for the Lagrangian and Eulerian accelerations in dependence of the Richardson number Ri is given in the first row of data in Table V at nondimensional time $St = 10$. For unstratified shear flow with Ri = 0, the Lagrangian and Eulerian accelerations are almost decorrelated as indicated by $r = 0.0284$. With increasing stratification strength, the Pearson product-moment correlation coefficient increases
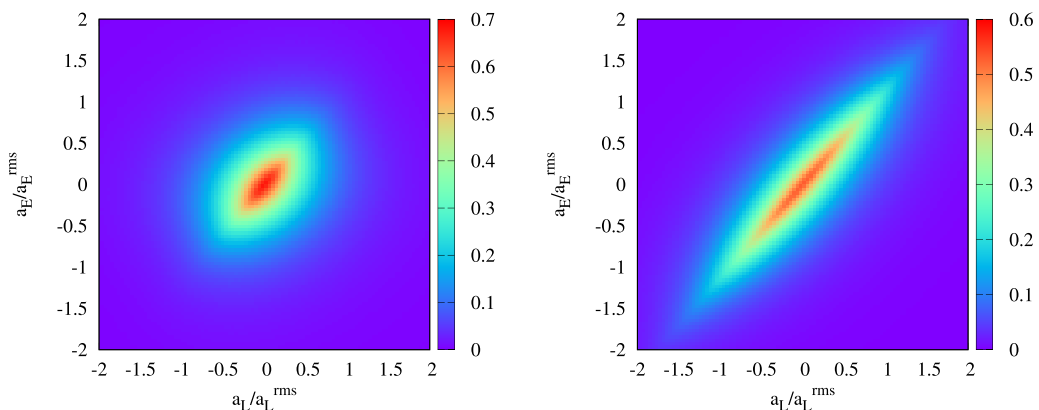

FIG. 5. Joint pdfs of Lagrangian acceleration $\boldsymbol{a}_L$ and Eulerian acceleration $\boldsymbol{a}_E$ for Richardson numbers Ri = 0.1 (left) and Ri = 1 (right) at nondimensional time $St = 10$ using a linear color scale.

TABLE V. Mean value of the cosine of the angle $\overline{\cos}$ and Pearson product-moment correlation coefficient r between the Lagrangian accelerations $\boldsymbol{a}_L$, the Eulerian acceleration $\boldsymbol{a}_E$, the convective contribution $\boldsymbol{a}_C = \boldsymbol{N}$, and the pressure gradient $\boldsymbol{a}_C = \boldsymbol{\Pi}$ at nondimensional time $St = 10$. The correlation coefficient is determined for all three components of the vector fields.

	Ri				
	0	0.1	0.2	0.5	1
$r(\boldsymbol{a}_L, \boldsymbol{a}_E)$	0.0284	0.0510	0.0882	0.2852	0.6634
$r(\boldsymbol{a}_L, \boldsymbol{a}_C)$	0.5823	0.6205	0.6232	0.5493	0.2741
$r(\boldsymbol{a}_E, \boldsymbol{a}_C)$	-0.7961	-0.7516	-0.7241	-0.6443	-0.5378
$r(\boldsymbol{a}_L, \boldsymbol{a}_P)$	-0.9728	-0.9545	-0.9211	-0.7014	-0.2843
$\overline{\cos}(\boldsymbol{a}_L, \boldsymbol{a}_E)$	0.1617	0.1957	0.2397	0.4347	0.7033
$\overline{\cos}(\boldsymbol{a}_L, \boldsymbol{a}_C)$	0.4199	0.4579	0.4582	0.3749	0.1964
$\overline{\cos}(\boldsymbol{a}_E, \boldsymbol{a}_C)$	-0.6573	-0.5945	-0.5563	-0.4561	-0.3538
$\overline{\cos}(\boldsymbol{a}_L, \boldsymbol{a}_P)$	-0.9110	-0.8761	-0.8157	-0.5273	-0.2659

monotonically. A high value of $r = 0.6634$ is observed for Ri = 1. This can be explained by the decreasing importance of the nonlinearity, quantified by the decreasing Reynolds number.

To provide further information, geometrical statistics are performed and the vector alignment properties of the different acceleration contributions are studied, as introduced in Sec. II E. For different Richardson numbers we consider the pdf of the cosine of the angle of two acceleration vectors, shown in Fig. 6, the mean value of the cosine as a quantitative measure, and the correlation coefficient, assembled in Table V. The choice of the cosine is motivated by the fact that for random fields in three dimensions the cosine of the angle is uniformly distributed and not the angle itself. Figure 6 (bottom left) shows a strong antialignment of the Eulerian acceleration $\boldsymbol{a}_E$ and the convective term $\boldsymbol{a}_C = \boldsymbol{N}$ reflected in a peak in the pdf at $\cos = -1$, corresponding to an angle of $180°$. This explains why the Lagrangian acceleration is smaller than the Eulerian one and also smaller than the convective term, as the antialignment implies that the two vectors $\boldsymbol{a}_E$ and $\boldsymbol{a}_C = \boldsymbol{N}$ are antiparallel. The Lagrangian acceleration $\boldsymbol{a}_L$ and the pressure gradient $\boldsymbol{\Pi}$ in Fig. 6 (bottom right) even show a stronger antialignment, which confirms that the negative pressure gradient is the driving force of the flow dynamics. In both cases the antialignment is most pronounced for Ri = 0 and becomes weaker for increasing Richardson numbers. This can be further quantified by the mean values of the cosine of the angle and also the correlation coefficient between the two vectors; the results are listed in Table V.

The Lagrangian acceleration is positively aligned with the Eulerian one (Fig. 6, top left) and also with the convective acceleration (Fig. 6, top right). For $\boldsymbol{a}_E$ this alignment becomes stronger with increasing Richardson number, while for $\boldsymbol{a}_C$ it becomes weaker, as the nonlinear term diminishes. These results are consistent with those of Tsinober et al. [1] obtained for isotropic turbulence, in the case of $Re_\lambda = 141$ (compared to our value for unstratified shear flow, 157). For example, for the average cosine of the angle between a_L and a_E Tsinober et al. [1] report a value of 0.105 (for unstratified shear flow we find 0.162); for a_L and a_C, 0.353 (0.420); and for a_E and a_C, -0.762 (-0.657).

Let us also mention that Tsinober et al. [1] showed that Gaussian random fields satisfy similar alignment properties for $\boldsymbol{a}_E$ and $\boldsymbol{a}_C = \boldsymbol{N}$ and concluded that this is essentially a kinematic effect.

Figure 7 presents the scale-dependent pdfs of the Lagrangian acceleration $\boldsymbol{a}_L$ (left) and Eulerian acceleration $\boldsymbol{a}_E$ (right) for two cases with Ri = 0.1 (top) and Ri = 1 (bottom) at nondimensional time $St = 10$. The pdfs have stretched-exponential shapes and the tails become heavier with increasing scale index j or decreasing scale of the turbulent motion. For the weakly stratified case with Ri = 0.1, the tails of the Lagrangian acceleration are generally heavier than those of the Eulerian acceleration. For the strongly stratified case with Ri = 1, however, the tails of the Eulerian
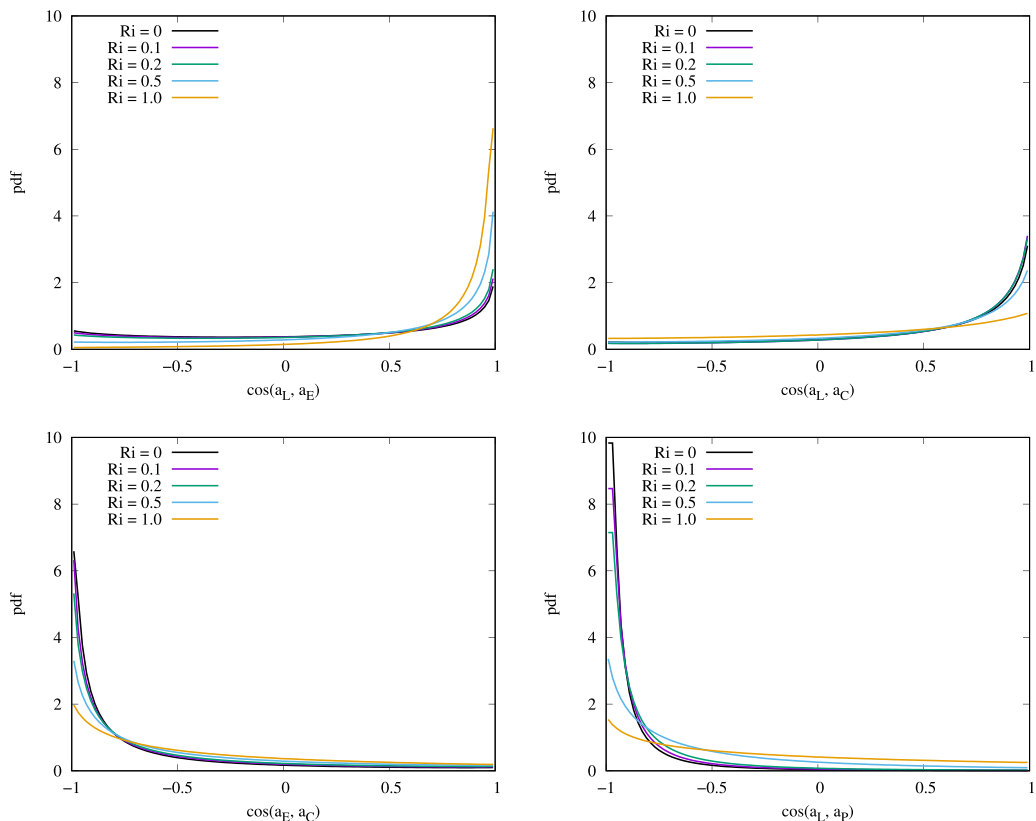
FIG. 6. Pdfs of the cosine of the angles between different acceleration contributions: $\cos(a_L, a_E)$ (top left), $\cos(a_L, a_C)$ (top right), $\cos(a_E, a_C)$ (bottom left), and $\cos(a_L, a_P)$ (bottom right) for different Ri values at nondimensional time $St = 10$.

acceleration are generally heavier than those of their Lagrangian counterpart. This observation reflects the trend for the total acceleration pdfs with increasing Richardson number discussed above.

In order to quantify the above observations, scale-dependent statistics are listed in Tables VI and VII for two cases with Richardson numbers Ri = 0.1 and Ri = 1, respectively. While the magnitude of the total Eulerian acceleration a_E is larger than the magnitude of the total Lagrangian acceleration a_L, the ordering is reversed for the accelerations at some scales of the turbulent motion. For the case with Ri = 0.1, the original ordering holds at the scale with the largest magnitude, which is $j = 6$

TABLE VI. Scale-dependent Lagrangian and Eulerian acceleration statistics for Ri = 0.1 at nondimensional time $St = 10$ showing the rms of the Lagrangian and Eulerian acceleration, a_E and a_L, and the flatness, Fl_{a_E} and Fl_{a_L}, for the total and the scale-dependent contributions at scale 2^{-j}.

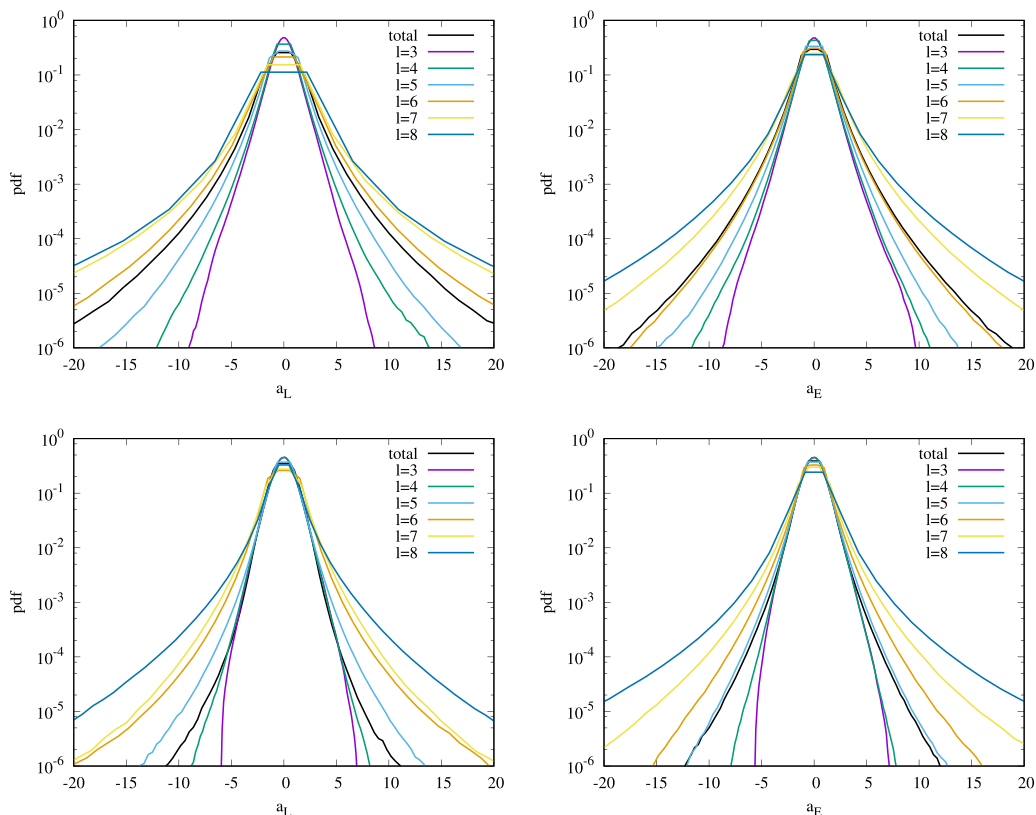| | | | | | | j | | | | |
	Total	0	1	2	3	4	5	6	7	8
a_L	9.833	0.156	0.361	0.769	1.787	3.672	5.666	5.773	3.491	1.280
Fl_{a_L}	26.041	4.933	3.468	4.706	4.968	6.844	10.979	39.138	119.480	252.821
a_E	11.689	0.150	0.360	0.682	1.589	3.477	6.026	7.137	5.344	2.364
Fl_{a_E}	13.413	4.296	3.304	4.103	5.061	5.981	8.114	12.607	27.600	65.829

FIG. 7. Scale-dependent normalized pdfs of Lagrangian acceleration $\boldsymbol{a}_L$ (left) and Eulerian acceleration $\boldsymbol{a}_E$ (right) for Richardson numbers Ri = 0.1 (top) and Ri = 1 (bottom) at nondimensional time $St = 10$. Note that the flat sections in the pdfs around 0 are artifacts of an even number of bins chosen in the computation of the pdfs. Additionally, pdfs of quantities with large variances only show fewer bins in the figure.

for both accelerations. At that scale, the pdfs of the total accelerations are also most similar to the pdfs of the accelerations at that scale. For the case with Ri = 1, the ordering observed for the magnitudes of the total accelerations holds more generally at different scales of the turbulent motion. The pdfs of the total accelerations are again most similar at the scales with the largest magnitudes, which are $j = 4$ for the Lagrangian acceleration and $j = 5$ for the Eulerian acceleration. The flatness of the accelerations generally increases with scale index j, indicating more intermittency at the

TABLE VII. Scale-dependent Lagrangian and Eulerian acceleration statistics for Ri = 1 at nondimensional time $St = 10$ showing the rms of the Lagrangian and Eulerian acceleration, a_E and a_L, and the flatness, Fl_{a_E} and Fl_{a_L}.

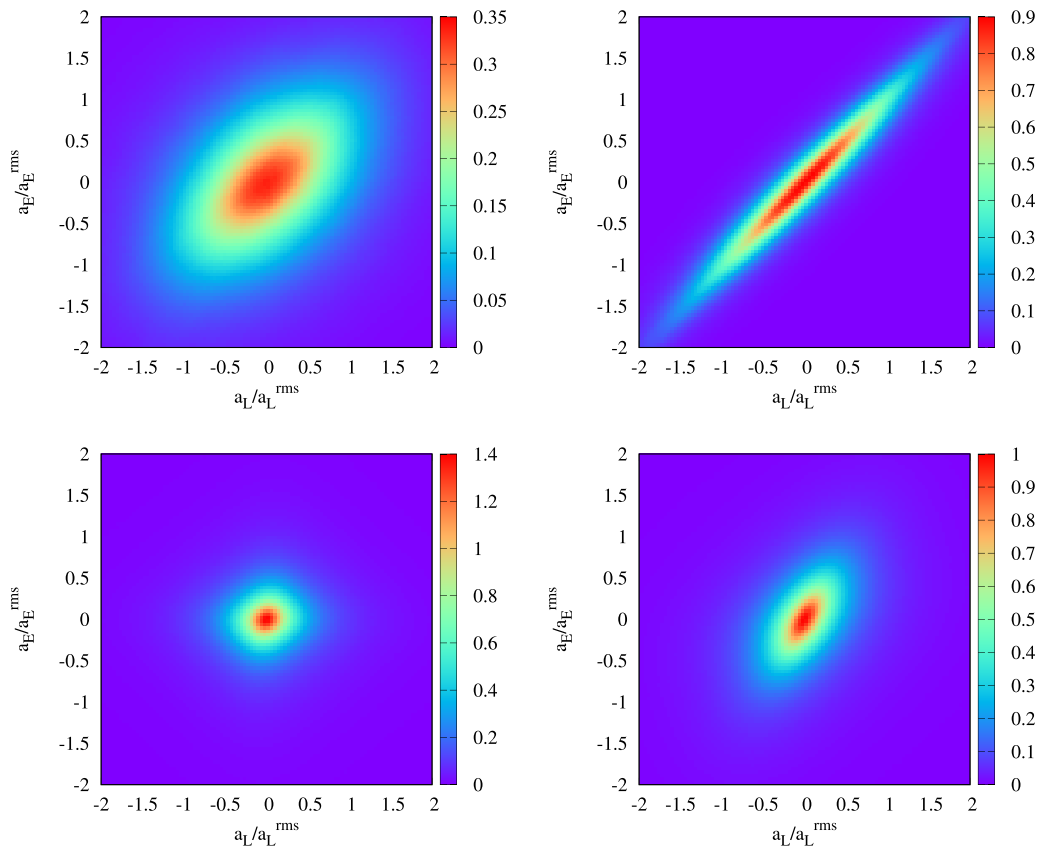|					j					
	Total	0	1	2	3	4	5	6	7	8
a_L	0.942	0.079	0.257	0.328	0.405	0.450	0.435	0.336	0.190	0.058
Fl_{a_L}	4.111	5.690	3.210	4.042	4.064	4.248	6.316	11.850	15.906	38.999
a_E	1.075	0.079	0.257	0.330	0.410	0.473	0.530	0.483	0.254	0.062
Fl_{a_E}	5.691	5.700	3.210	4.021	4.034	4.166	6.524	10.411	21.338	66.034

FIG. 8. Scale-dependent joint pdfs of Lagrangian acceleration $\boldsymbol{a}_L$ and Eulerian acceleration $\boldsymbol{a}_E$ for Richardson numbers Ri = 0.1 (left) and Ri = 1 (right) and at large scale with scale index $j = 3$ (top) and at small scale with $j = 7$ (bottom) at nondimensional time $St = 10$ using a linear color scale.

smallest scales of motion. Note that for the Lagrangian acceleration, flatness values close to 3 are observed for the larger scales with $j = 1$, indicating that the Lagrangian acceleration at large scale is mainly determined by linear effects.

Figure 8 shows the scale-dependent joint pdfs of the Lagrangian and Eulerian accelerations for two cases with Ri = 0.1 (left) and Ri = 1 (right) as well as at large scale with scale index $j = 3$ (top) and at small scale with $j = 7$ (bottom) at nondimensional time $St = 10$. Consistent with the observation for the total accelerations discussed above, the correlation increases with the stratification strength at the two scales shown. In addition, the correlation decreases with increasing scale index j or decreasing scale of the turbulent motion considered.

This observation is shown more quantitatively using the Pearson product-moment correlation coefficient in Table VIII. The correlation coefficient tends to increase with increasing Richardson number Ri. Similarly, at all Richardson numbers, the correlation coefficient decreases with decreasing scale or increasing scale index j. The components at the largest scale index j or smallest scale of motion are characterized by very high flatness values. This indicates strong intermittency present in the motion, with the localized activity impacting the correlation coefficient. Note that with increasing Ri, the Taylor microscale Reynolds number Re_λ decreases. Starting from the same initial conditions, an increase in the Richardson number Ri necessarily results in a decrease in the Taylor microscale Reynolds number Re_λ due to the effect of stratification. Hence it is difficult to

TABLE VIII. Pearson product-moment correlation coefficient r for the scale-dependent Lagrangian and Eulerian accelerations at nondimensional time $St = 10$. The correlation coefficient is determined for all three components of the accelerations.

	Ri				
	0	0.1	0.2	0.5	1
$r\,(j = 0)$	0.8584	0.9716	0.9892	0.9969	0.9995
$r\,(j = 1)$	0.8065	0.9347	0.9625	0.9957	0.9990
$r\,(j = 2)$	0.5208	0.6709	0.8287	0.9728	0.9921
$r\,(j = 3)$	0.1988	0.3427	0.5072	0.8257	0.9512
$r\,(j = 4)$	0.0884	0.1380	0.2141	0.4959	0.7765
$r\,(j = 5)$	0.0308	0.0478	0.0739	0.2002	0.4528
$r\,(j = 6)$	0.0116	0.0196	0.0304	0.0993	0.2919
$r\,(j = 7)$	0.0037	0.0097	0.0248	0.1248	0.3337
$r\,(j = 8)$	-0.0052	0.0200	0.0261	0.1707	0.3837

determine whether the origin of the increased intermittency is due to the increased stratification or decreased Re_λ, as the two effects are linked.

C. Lagrangian and Eulerian time rates of change of fluctuating density

The time rates of change of fluctuating density can also be defined using Lagrangian and Eulerian approaches as

$$s_L = \frac{\partial \rho}{\partial t} + \boldsymbol{u} \cdot \nabla \rho \quad \text{and} \quad s_E = \frac{\partial \rho}{\partial t}, \tag{20}$$

respectively.

Figure 9 (top) shows the pdfs of the Lagrangian time rate of change of fluctuating density (left) and of the corresponding Eulerian time rate of change (right). The difference in the pdfs of the time rates of change is much more pronounced than the difference obtained for the accelerations. Figure 9 (bottom) shows the normalized pdfs of the two time rates of change. While the shape of the Eulerian time rate of change pdf is again found to be stretched exponential, the Lagrangian time rate of change pdf has a more Gaussian shape. The extreme values of the Eulerian time rate of change of fluctuating density are substantially larger than those of the Lagrangian time rate of change.

Tables II and III, respectively, provide the dependence of the magnitudes of the Lagrangian and Eulerian time rates of change on the Richardson number Ri. Note that for Ri = 0, the density is a passive scalar (zero gravity) with a mean gradient. Again, the magnitude of s_E always remains larger than the magnitude of s_L, consistent with the findings for the accelerations.

The flatnesses of the Lagrangian and Eulerian time rates of change are also listed in Tables II and III, respectively. The flatness of s_E is always larger than that of s_L and their values generally decrease with increasing Ri. For strong stratification, the flatness of the Lagrangian time rate of change assumes values of around 3 for Ri = 1, while the Eulerian time rate of change yields a value of 5.475.

Figure 10 shows pdfs of the buoyancy term (left) and advection term (right) in the advection-diffusion equation for fluctuating density. The buoyancy term pdf has a Gaussian shape, as it is linearly related to the fluctuating density. Its variance increases with increasing Ri, because the stratification rate S_ρ increases. The more Gaussian shape of the Lagrangian time rate of change of fluctuating density can be explained by the lack of a quadratic term in the advection-diffusion equation for fluctuating density. The large difference observed between the Lagrangian and the Eulerian time rates of change of fluctuating density is due to the advection term.
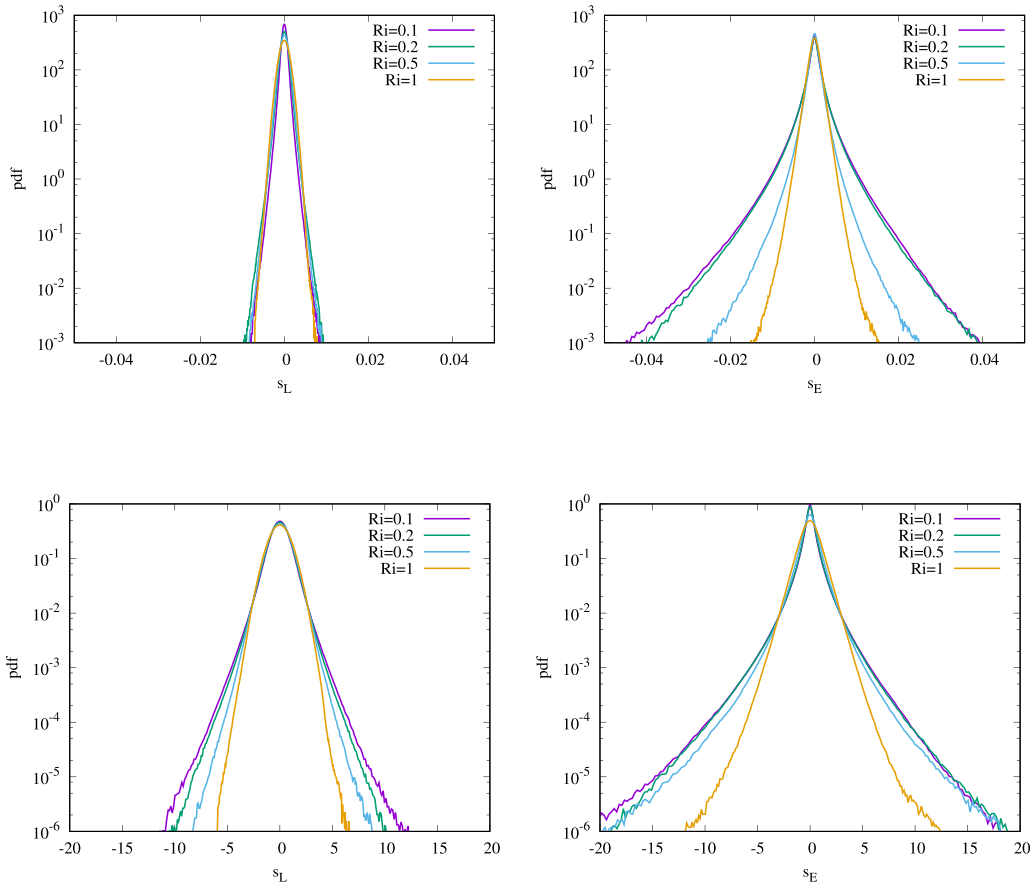
FIG. 9. Pdfs (top) and normalized pdfs (bottom) of Lagrangian time rate of change of fluctuating density s_L (left) and Eulerian time rate of change s_E (right) at nondimensional time $St = 10$.
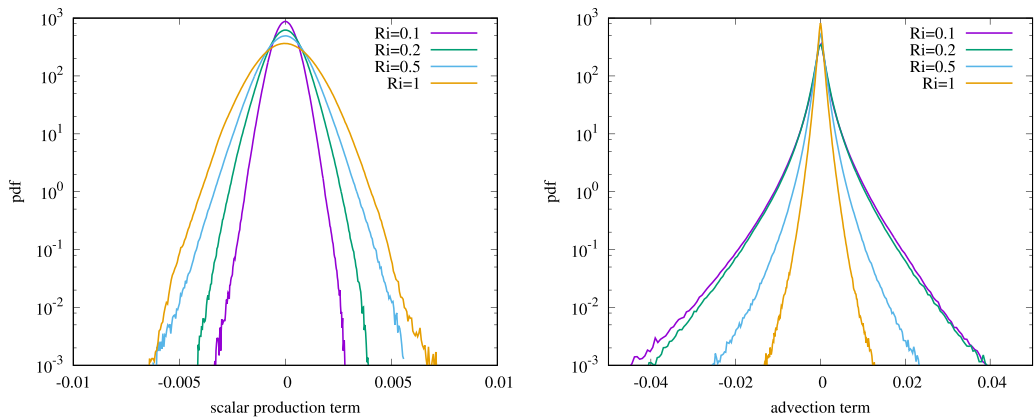

FIG. 10. Pdfs of the buoyancy (left) and advection (right) terms in the advection-diffusion equation for fluctuating density at nondimensional time $St = 10$.

IV. CONCLUSIONS

A series of direct numerical simulations was performed in order to study the Lagrangian and Eulerian acceleration properties in stably stratified turbulent shear flows. With increasing Richardson number Ri, the evolution of the turbulent kinetic energy K changes from growth to decay and the variances of the Lagrangian acceleration $\boldsymbol{a}_L$ and the Eulerian acceleration $\boldsymbol{a}_E$ decrease. The acceleration pdfs were observed to have a stretched-exponential symmetric shape and the flatness decreases with increasing Ri.

We studied the cancellation of Eulerian and convective accelerations of fluid particles using geometrical statistics of the vector quantities. We found a strong preference for the antialignment of both vectors, which decreases with the Richardson number. This cancellation explains why the variance of the Lagrangian acceleration is smaller than its Eulerian counterpart and it supports, according to Tsinober *et al.* [1], who performed similar analyses for isotropic turbulence, the random Taylor hypothesis for shear flow, which, however, becomes weaker with increasing stratification. Nevertheless, we do not find an order-of-magnitude difference in the acceleration variances, as predicted by Tennekes [11] for isotropic turbulence and necessary so that the random Taylor hypothesis strictly holds. These findings are in agreement with Lin [12], who showed that Taylor's hypothesis in general does not hold for shear flow. Analyzing the alignment properties of the scale-dependent contributions of the acceleration is an interesting perspective for future work, already in the context of isotropic turbulence. This would allow us to check whether the hypothesis holds for shear flows at least at small scales.

An estimation of the variances of the Lagrangian and Eulerian accelerations has been derived from the Navier-Stokes equations which requires the ratio of potential to kinetic energy. A comparison of the estimation with results from the direct numerical simulations showed good agreement for the considered range of Richardson numbers.

The pdfs of the pressure-gradient and advection terms in the Navier-Stokes equation, which are both quadratic terms, also have stretched-exponential shapes. The Lagrangian and Eulerian accelerations are mainly determined by the pressure-gradient and advection terms, respectively. While the quadratic terms are dominant for small Ri, their dominance is somewhat diminished for large Ri. The pdfs of the shear and buoyancy terms in the Navier-Stokes equation, which are both linear terms, were observed to have a Gaussian shape. While the variance of the shear term decreases with Ri, the variance of the buoyancy term increases with Ri.

In addition, the Lagrangian and Eulerian time rates of change of fluctuating density and of fluctuating vorticity (see Appendix A) were considered. For both quantities, the Eulerian time rates of change showed substantially larger extreme values than their Lagrangian counterparts. Due to the lack of a quadratic term on the right-hand side of the advection-diffusion equation for fluctuating density, the pdf of the Lagrangian time rate of change has an almost-Gaussian shape, while the pdf of the Eulerian time rate of change was observed to have exponential to stretched-exponential shapes. For fluctuating vorticity we found that the Lagrangian time rate of change is mainly determined by the vortex streching and tilting term.

A scale-dependent analysis using orthogonal wavelet decomposition provided insight into the intermittency of the Lagrangian and Eulerian accelerations. At small scales of the turbulent motion, the pdfs exhibit heavy tails, resulting in very large flatness values and corresponding intermittency. The correlation between the Lagrangian and the Eulerian accelerations has likewise been analyzed and we found stronger correlation at large scales of turbulent motion as well as with increasing Richardson number. At small scales this correlation is substantially reduced.

For rotating and sheared homogeneous turbulence, Salhi *et al.* [28] observed a dominance of linear terms in cases with strong rotation and the flatness of the Lagrangian acceleration assumes a value of about 3. This observation suggests that linear theory can accurately describe the properties of such flows. In the present study, however, the flatness never reaches values close to 3, even for very large Richardson numbers. Hence, linear theory should not yield agreement with direct
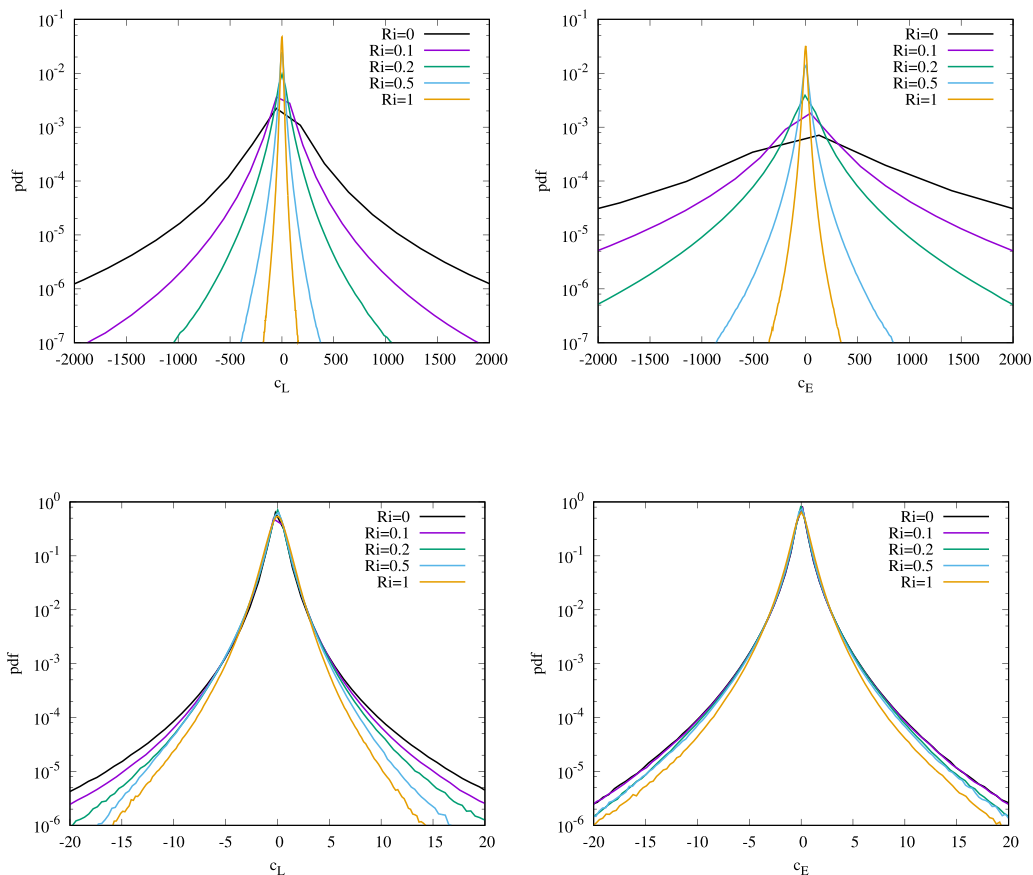
FIG. 11. Pdfs (top) and normalized pdfs (bottom) of Lagrangian time rate of change of vorticity c_L (left) and Eulerian time rate of change c_E (right) at nondimensional time $St = 10$. Note that pdfs for the vector quantities are shown.

numerical simulation results. Indeed, Hanazaki and Hunt [23] found important differences between linear theory and the fully nonlinear evolution of homogeneous turbulence in stratified shear flows.

Perspectives for future work include a componentwise analysis of the Lagrangian and Eulerian acceleration, a more detailed scalewise decomposition of the geometric properties of the accelerations, and corresponding terms for the vorticity evolution.
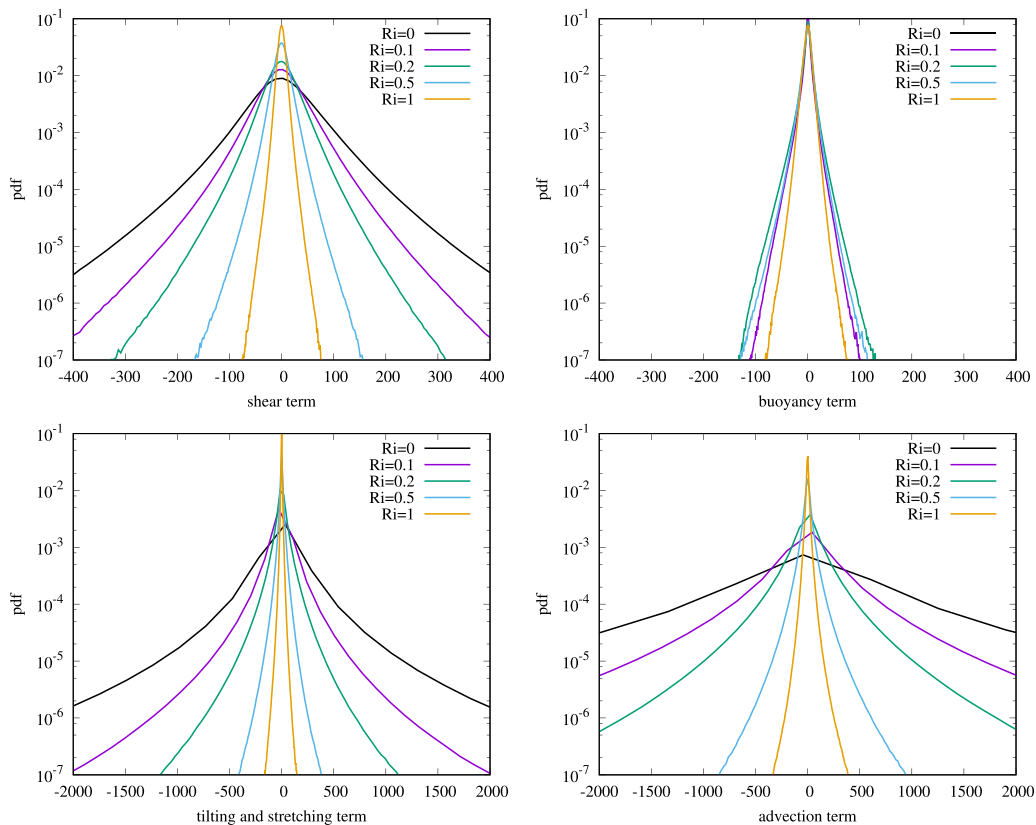
FIG. 12. Pdfs of the shear (top left), buoyancy (top right), vortex tilting and stretching (bottom left), and advection (bottom right) terms in the vorticity equation at nondimensional time $St = 10$.

APPENDIX A: LAGRANGIAN AND EULERIAN TIME RATES OF CHANGE OF FLUCTUATING VORTICITY

The Lagrangian and Eulerian time rates of change of fluctuating vorticity $\boldsymbol{\omega}$ are defined as

$$\boldsymbol{c}_L = \frac{\partial \boldsymbol{\omega}}{\partial t} + \boldsymbol{u} \cdot \nabla \boldsymbol{\omega} \quad \text{and} \quad \boldsymbol{c}_E = \frac{\partial \boldsymbol{\omega}}{\partial t}, \tag{A1}$$

respectively. This definition is analogous to the definition for the Lagrangian and Eulerian accelerations in order to enable a comparison between the accelerations and the vorticity time rate of change statistics. Again, the analysis is performed at the nondimensional time $St = 10$.

Figure 11 (top) shows the pdfs of the Lagrangian time rate of change $\boldsymbol{c}_L$ (left) and of the Eulerian time rate of change $\boldsymbol{c}_E$ (right). Similarly to the accelerations, pdfs with stretched-exponential shapes are observed for both time rates of change and a strong and similar influence on the Richardson number Ri is obtained. Again, stronger extreme values are obtained for the Eulerian time rate of change, but the difference from the Lagrangian time rate of change is much more pronounced here compared to the accelerations. Figure 11 (bottom) shows the normalized pdfs of the two time rates of change. Again, for a core region of about five standard deviations, both the Lagrangian and the Eulerian time rates of change have an approximately similar shape. For small Richardson numbers Ri, the tails of the Lagrangian time rate of change are heavier than those of their Eulerian counterparts. However, this ordering is reversed at larger Ri.
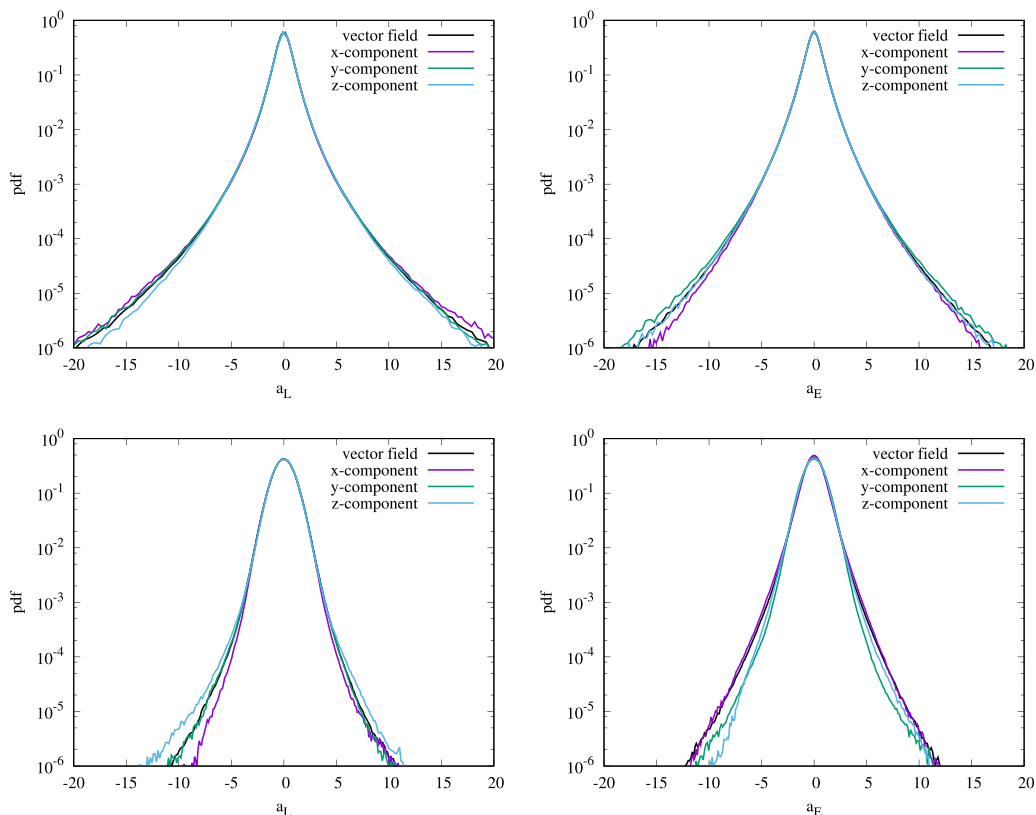
FIG. 13. Comparison of normalized vector pdfs with their corresponding normalized component pdfs for Lagrangian acceleration (left) and Eulerian acceleration (right) for Ri = 0.1 (top) and Ri = 1 (bottom) at nondimensional time $St = 10$.

The magnitudes of the Lagrangian and Eulerian vorticity time rates of change are listed in Tables II and III, respectively. Similarly to the magnitudes of the accelerations, the magnitudes of both time rates of change decrease with increasing Ri and the variance of c_E always remains larger than the variance of c_L. This difference in the magnitudes for the vorticity time rate of change pdfs is much more pronounced than that of the accelerations. The heavier tails observed for the pdf of c_L compared to c_E at small Ri results in a larger flatness of the Lagrangian time rate of change pdf compared to its Eulerian counterpart. Again, the ordering of the flatness values is reversed at larger Ri. While the flatness values decrease with increasing Ri, the flatness is again observed to level off at a value of approximately 5, well above the value of 3 expected for a Gaussian pdf. Hence, some nonlinearity is still present even in the case of strongly suppressed turbulence in strongly stratified flows.

Figure 12 shows pdfs of the shear term (top left), the buoyancy term (top right), the vortex tilting and stretching term (bottom left), and the advection term (bottom right) in the vorticity equation. The shear and buoyancy terms depend linearly on the curl of fluctuating velocity components and fluctuating density, respectively. Similarly to the respective terms in the Navier-Stokes equation, the magnitude of the shear term decreases with increasing Ri and the magnitude of the buoyancy term increases. The pdfs of the vortex tilting and stretching term and the advection term show stretched-exponential shapes due to the quadratic nature of the terms. The magnitudes of both terms decrease with increasing Ri. For small Ri, the vortex tilting and stretching term as well as the advection term clearly dominates the shear and buoyancy terms, but this dominance is again reduced for large Ri. In the case of vorticity, the vortex tilting and stretching term is the generally dominant

contribution to the Lagrangian time rate of change, while the advection term is important for the Eulerian time rate of change.

APPENDIX B: LAGRANGIAN AND EULERIAN COMPONENT pdfs

While the text exclusively discusses the properties of vector pdfs, this Appendix presents component pdfs of the Lagrangian and Eulerian accelerations in order to address their anisotropy in turbulent stratified shear flow. Figure 13 compares the vector pdfs with their x-, y-, and z-component pdfs for Lagrangian acceleration (left) and Eulerian acceleration (right) for two cases with weak stratification with Ri = 0.1 (top) and with strong stratification with Ri = 1 (bottom). All pdfs show similar shapes and the flow anisotropy is reflected in the variances. A similar observation holds for the pdfs of Lagrangian and Eulerian time rates of change of fluctuating vorticity (not shown here).

The ratios of the component variances to the corresponding vector variances of the Lagrangian and Eulerian accelerations are listed in Tables II and III, respectively. For small Richardson numbers Ri, the variance ratios show a near-equipartition between the three components for both the Lagrangian and the Eulerian accelerations. For large Ri, however, the ratio of the vertical variances to the vector variances increases due to the direct impact of the buoyancy term in the vertical component of the Navier-Stokes equation. Figure 2 shows that the ratio of potential to kinetic energy increases with increasing Ri. Hence the buoyancy term impacts particularly the vertical component of the accelerations.

---

[1] A. Tsinober, P. Vedula, and P. K. Yeung, Random Taylor hypothesis and the behavior of local and convective accelerations in isotropic turbulence, Phys. Fluids **13**, 1974 (2001).

[2] A. Tsinober, *An Informal Introduction to Turbulence* (Kluwer Academic, Dordrecht, 2001).

[3] W. Heisenberg, Zur statistischen theorie der turbulenz, Z. Phys. **124**, 628 (1948).

[4] A. M. Yaglom, On the acceleration field in a turbulent flow, C.R. Akad. URSS **67**, 795 (1949).

[5] S. B. Pope, Lagrangian pdf methods for turbulent flows, Annu. Rev. Fluid Mech. **26**, 23 (1994).

[6] A. La Porta, G. A. Voth, A. M. Crawford, J. Alexander, and E. Bodenschatz, Fluid particle accelerations in fully developed turbulence, Nature **409**, 1017 (2001).

[7] P. K. Yeung and S.B. Pope, Lagrangian statistics from direct numerical simulations of isotropic turbulence, J. Fluid Mech. **207**, 531 (1989).

[8] P. K. Yeung, Lagrangian investigations of turbulence, Annu. Rev. Fluid Mech. **34**, 115 (2002).

[9] F. Toschi and E. Bodenschatz, Lagrangian properties of particles in turbulence, Annu. Rev. Fluid Mech. **41**, 375 (2009).

[10] M. Pinsky, A. Khain, and A. Tsinober, Accelerations in isotropic and homogeneous turbulence and Taylor's hypothesis, Phys. Fluids **12**, 3195 (2000).

[11] H. Tennekes, Eulerian and Lagrangian time microscales in isotropic turbulence, J. Fluid Mech. **67**, 561 (1975).

[12] C. C. Lin, On Taylor's hypothesis and the acceleration terms in the Navier-Stokes equation, Q. Appl. Math. **10**, 295 (1953).

[13] G. He, G. Jin, and Y. Yang, Space-time correlations and dynamic coupling in turbulent flows, Annu. Rev. Fluid Mech. **49**, 51 (2017).

[14] S. Komori, H. Ueda, F. Ogino, and T. Mizushina, Turbulence structure in stably stratified open-channel flow, J. Fluid Mech. **130**, 13 (1983).

[15] J. J. Rohr, E. C. Itsweire, K. N. Helland, and C. W. Van Atta, Growth and decay of turbulence in a stably stratified shear flow, J. Fluid Mech. **195**, 77 (1988).

[16] P. S. Piccirillo and C. W. Van Atta, The evolution of a uniformly sheared thermally stratified turbulent flow, J. Fluid Mech. **334**, 61 (1997).

[17] K. H. Keller and C. W. Van Atta, An experimental investigation of the vertical temperature structure of homogeneous stratified shear turbulence, J. Fluid Mech. **425**, 1 (2000).

[18] T. Gerz, U. Schumann, and S. E. Elghobashi, Direct numerical simulation of stratified homogeneous turbulent shear flows, J. Fluid Mech. **200**, 563 (1989).

[19] S. E. Holt, J. R. Koseff, and J. H. Ferziger, A numerical study of the evolution and structure of homogeneous stably stratified sheared turbulence, J. Fluid Mech. **237**, 499 (1992).

[20] F. G. Jacobitz, S. Sarkar, and C. W. Van Atta, Direct numerical simulations of the turbulence evolution in a uniformly sheared and stably stratified flow, J. Fluid Mech. **342**, 231 (1997).

[21] F. G. Jacobitz, A comparison of the turbulence evolution in a stratified fluid with vertical or horizontal shear, J. Turbul. **3**, N55 (2002).

[22] G. D. Portwood, A Study on Homogeneous Sheared Stably Stratified Turbulence, Ph.D. thesis, University of Massachusetts, Amherst, 2019.

[23] H. Hanazaki and J. C. R. Hunt, Structure of unsteady stably stratified turbulence with mean shear, J. Fluid Mech. **507**, 1 (2004).

[24] H. Salehipour, W. R. Peltier, and A. Mashayek, Turbulent diapycnal mixing in stratified shear flows: The influence of Prandtl number on mixing efficiency and transition at high Reynolds number, J. Fluid Mech. **773**, 178 (2015).

[25] S. K. Venayagamoorthy and J. R. Koseff, On the flux Richardson number in stably stratified turbulence, J. Fluid Mech. **798**, R1 (2016).

[26] M. C. Gregg, E. A. D'Asaro, J. J. Riley, and E. Kunze, Mixing efficiency in the ocean, Annu. Rev. Mar. Sci. **10**, 443 (2018).

[27] F. G. Jacobitz, K. Schneider, W. J. T. Bos, and M. Farge, Structure of sheared and rotating turbulence: Multiscale statistics of Lagrangian and Eulerian accelerations and passive scalar dynamics, Phys. Rev. E **93**, 013113 (2016).

[28] A. Salhi, F. G. Jacobitz, K. Schneider, and C. Cambon, Nonlinear dynamics and anisotropic structure of rotating sheared turbulence, Phys. Rev. E **89**, 013020 (2014).

[29] R. S. Rogallo, Numerical experiments in homogeneous turbulence, Technical Report TM 81315 (NASA Ames Research Center, Moffett Field, CA, 1981).

[30] T. Hou and R. Li, Computing nearly singular solutions using pseudo-spectral methods, J. Comput. Phys. **226**, 379 (2007).

[31] S. Mallat, *A Wavelet Tour of Signal Processing* (Academic Press, San Diego, CA, 1998).

[32] M. Farge and K. Schneider, Wavelet transforms and their applications to MHD and plasma turbulence: A review, J. Plasma Phys. **81**, 435810602 (2015).

[33] K. Schneider, M. Farge, and N. Kevlahan, Spatial intermittency in two–dimensional turbulence: a wavelet approach, in *Woods Hole Mathematics, Perspectives in Mathematics and Physics*, Vol. 34, edited by N. Tongring and R.C. Penner (World Scientific, Singapore, 2004), pp. 302–328.

[34] A. S. Monin and A. M. Yaglom, *Statistical Fluid Mechanics: The Mechanics of Turbulence*, Vol. I (MIT Press, Cambridge, MA, 1971).